Solar Energy 270 (2024) 112377

Contents lists available at ScienceDirect

Solar Energy

journal homepage: www.elsevier.com/locate/solener

An adaptive power smoothing approach based on artificial potential field for PV plant with hybrid energy storage system

Xiangqiang Wu [a], Yue Wu [b], Zhongting Tang [a], Tamas Kerekes [a,*]

[a] Department of AAU Energy, Aalborg University, Aalborg 9220, Denmark
[b] School of Automation, Central South University, Changsha 410083, China

A R T I C L E I N F O

Keywords:
Power smoothing
Artificial potential field
Hybrid energy storage system
Battery degradation

A B S T R A C T

The increasing quantity of PV installation has brought great challenges to the grid owing to power fluctuations. Hybrid energy storage systems have been an effective solution to smooth out PV output power variations. In order to reduce the required capacity and extend the lifetime of the hybrid energy storage system, a two-stage self-adaptive smoothing approach based on the artificial potential field is proposed to decompose and allocate power among the grid, battery, and supercapacitor dynamically. In the ramp rate control stage, an unsymmetric artificial potential field method is used to regulate the cutoff frequency of a low-pass filter, so as to limit the PV power ramp rate within the prescribed range and allocate the power between the grid and the hybrid energy storage system. In the HESS power distribution stage, a symmetric artificial potential field is adopted to distribute power between the battery and supercapacitor by regulating the cutoff frequency of another low-pass filter. The effectiveness of the proposed strategy is validated through a case study based on real-world PV data in Denmark. The results show that the proposed method outperforms to reduce the over-smoothing effect and battery degradation, which can reduce battery loss by up to 17% to 49% compared to existing smoothing approaches.

1. Introduction

Integrating photovoltaic (PV) sources into the grid is a trend in progress, providing long-term environmental benefits and reducing system loss. However, due to the characteristics of stochastics and intermittency, PV power generation can bring some challenges or negative impacts to the grid. For example, in terms of grid operation, PV power fluctuation may induce voltage and frequency fluctuation at the point of common coupling, which may result in instability in weak grid conditions [1]. And power fluctuations can cause power imbalance, which affects the primary and secondary frequency regulation of the system [2]. In terms of economics, it is reported that rapid power changes will increase the operation cost of grid-connected conventional generators [3]. In order to ensure the quality and stability of the power system, power ramp rate control (PRRC) has been widely applied to many grid codes. Table 1 lists several common standards in different countries regarding PV power ramp rate (RR) constraints. It can be seen that PRRC is a mandatory requirement for the solar system, and most countries adopt 10 % of the rated PV capacity per minute. It is worth noticing that there can be more than one transmission system operator in a country, and the RR standards can be different regarding their power and voltage levels. In order to meet the requirement, flexible PRRC methods are needed for PV systems [4].

A lot of studies have investigated various RR control methods. Generally speaking, the RR methods can be divided into storage-based methods and storage-less methods [12]. However, storage-less methods, which are known as active power curtailment (APC) methods as well, rely on the accurate forecast of the solar irradiance to smooth out downward power fluctuation. Some studies like the sky camera method [13] and the ground-sensor-based method [14] with the deep reinforcement learning algorithm have been reported to improve forecasting accuracy. Nevertheless, the predictive APC algorithms have a high computation burden and require frequent calibration, which increases implementation difficulty. Usually, filter-based methods coupled with energy storage systems (ESS) are common solutions to smooth out power fluctuations [3]. ESS needs to provide power compensation to smooth the PV power ramp rate, which requires frequent charging/discharging. As a result, the degradation of ESS lifetime will lead to higher maintenance costs and replacement costs. Besides, one kind of ESS suffers from its limitations (e.g., power density, energy density,

* Corresponding author.
E-mail address: tak@energy.aau.dk (T. Kerekes).

https://doi.org/10.1016/j.solener.2024.112377
Received 21 July 2023; Received in revised form 25 December 2023; Accepted 25 January 2024
Available online 3 February 2024

Table 1
PV PRRC standards in different grid codes.

Country	Title	Constraint
Germany	Technical guideline, generating plants connected to the medium-voltage network [5]	10 %/min
UK	Distribution planning and connection code [6]	10 %/min
Ireland	EirGrid grid code [7]	30 MW/min
USA	Grid standards and codes [8]	30 MW/min
Egypt	Solar energy plants grid connection code [9]	10 %/min
China	Technical rule for photovoltaic power station connected to Power Grid [10]	10 %/min
South Africa	Grid connection code for renewable power plants connected to the electricity transmission system or the distribution system in South Africa [11]	2 %/min

lifetime), which hinders the performance improvements of ESS. Therefore, from the viewpoint of economics and technology, the hybrid energy storage system (HESS), which consists of different storage technologies, can take full advantage of complementary characteristics to decrease the total costs and improve the quality of grid-feeding power [15].

After determining the configuration of the PV system, a reasonable power allocation strategy is the key to smoothing the PV power fluctuations and distributing power among different energy storage elements. In state-of-the-art, the frequency decomposition method is the most commonly adopted approach in RR control with HESS applications [3]. The principle of the frequency decomposition method is to divide PV output power into three parts: low-frequency, intermediate-frequency, and high-frequency components, then the low-frequency power components are injected into the grid, and the intermediate-frequency and high-frequency components are injected into the slow storage elements (e.g., batteries) and fast storage elements (e.g., supercapacitors). In this way, the RR of PV power can be limited within a certain range, and the battery lifespan can be extended. In this context, methods based on low-pass filters (LPF) [16,17] and moving average (MA) filters [18,19] are most commonly used to decompose PV output power. Nevertheless, the time constant (TC) of LPF is hard to design considering different weather and operation conditions. Moreover, MA filters have the "memory effect", which relies on previous data to calculate the present value. Hence, though the power RR can be limited within the prescribed range, the above methods can inevitably oversmooth the PV power, which will increase the capacity of HESS and decrease the storage lifetime.

In order to achieve flexible control and prolong battery lifetime, some adaptive power allocation algorithms are proposed. In [20], the state of charge (SoC) of the supercapacitor (SC) is used to regulate the TC of LPF linearly in a standalone PV system, where the SC SoC is kept within a moderate range, but the battery lifetime is not considered. In [21], authors use a long short-term memory network to predict the next day's weather and initialize the TC value, then an LPF and a high-pass filter are used for RR control and power distribution, respectively, which outperforms the fixed TC LPF and MA in terms of battery lifetime. Wu, et al. [22] develop a fuzzy control function between the SC SoC and the LPF TC value, which dynamically regulates the power distribution. In addition, some studies decompose power signals and reconstruct them after filtering the high-frequency components, without using filters. For example, a wavelet package decomposition technique is adopted in [23] to decompose the output power and allocate different frequency components into the grid and HESS, respectively. But the wavelet decomposition method has no self-adaptive capacity, which will overuse energy storage. In [24], a variational mode decomposition (VMD) algorithm is used in wind power smoothing applications, but the mode mixing problem is not properly addressed. Xiao, et al. [25] propose a self-adaptive VMD algorithm by considering the influence of more intrinsic mode functions, which reduces the HESS capacity to some degree. Furthermore, some studies explore optimization-based methods [26–28] to minimize or maximize some objective function (e.g., system energy loss, economic benefits) through online or offline optimization algorithms. However, this kind of method apparently increases the computation and communication burden, which remains to be proven practical in industrial applications.

In summary, though there are a lot of studies about PV power smoothing with HESS, there are still some challenges. Specifically, (1) Most frequency decomposition-based approaches oversmooth the PV power, even though the RR limit is within the prescribed, thus additional flexible frequency decomposition approaches need to be further developed to decrease HESS capacity and extend battery lifetime. (2) Some existing studies only focus on the SoC limits, without considering power capacity limits, which is not practical. (3) Most studies ignore the dynamic battery aging caused by the current rate and frequency when discussing battery degradation, resulting in unguaranteed performance in practice.

To bridge these research gaps, this paper proposes a two-stage self-adaptive frequency decomposition approach based on artificial potential field (APF) to dynamically allocate the PV power among the grid, battery, and supercapacitor. The contributions of the paper are summarized as follows:

- An asymmetric APF-based filter is used to control the RR of PV output power, and a symmetric APF-based filter is used to allocate

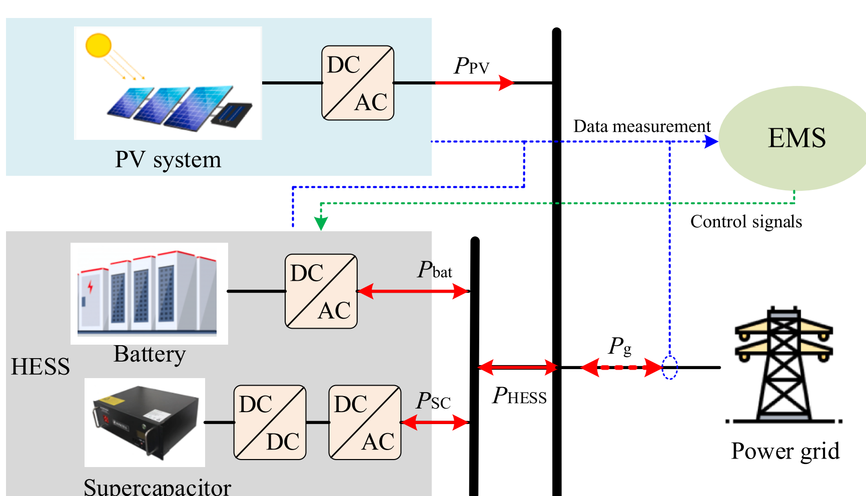

Fig. 1. System structure and information flow of PV-HESS system.

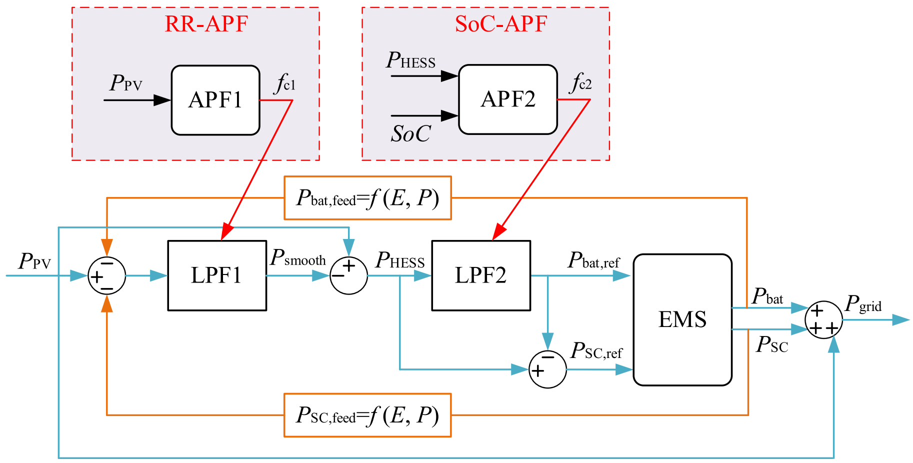

Fig. 2. Overall control diagram of the PV-HESS system.

intermediate-frequency and high-frequency power for the battery and SC, respectively. The TCs of two LPFs are regulated individually, resulting in lower HESS capacity and less battery stress.

- Instead of cycle models, a dynamic battery aging model is adopted to qualify the lifetime extension, which reflects the influence of high-frequency currents and highlights the importance of self-adaptive power allocation methods.
- This method is a real-time method with power capacity limits and charging/discharging efficiency considered, which does not rely on power predictions or weather forecasts. Thus, the calculation and communication burden can be reduced significantly.

The remainder of this paper is organized as follows: Section 2 introduces the HESS-integrated PV system, including the PV and battery model. Section 3 introduces the proposed APF-based frequency decomposition approach for power smoothing and allocation. Case studies and discussions are carried out in Section 4. Finally, Section 5 concludes this paper.

2. Architecture of PV-HESS system

2.1. PV-HESS system configuration

Fig. 1 shows the system topology and information flow of the PV-HESS system. In this paper, the HESS consists of the Li-ion battery and SC, and they connect the same bus through individual DC/AC converters, which serve as an active topology[29] . It should be noted that the SC has a DC/DC stage to ensure the DC voltage of the inverter, while the battery connects to the inverter directly due to its voltage characteristics [30]. The PV and HESS are integrated with AC-parallel, where the PV and HESS are connected to the same AC bus [31]. P_{pv} denotes the PV active power, and P_{HESS} is the HESS power, which is the sum of battery power P_{bat} and SC power P_{SC}. P_{grid} is the grid power, which is the sum of PV power and HESS power. The energy management system (EMS) collects real-time information (e.g., power, SoC) of PV, HESS, and grid. Then, after processing collected data, EMS sends control signals to adjust HESS power, thereby smoothing the PV power fluctuation and ensuring a stable operation of the PV-HESS system.

Fig. 2 further shows the control diagram of the PV-HESS system. Firstly, the PV power is measured by PV converters, and through the first LPF block, the smoothed power P_{smooth} is obtained. The power shortage or excess power P_{HESS} is compensated by the battery and SC. Then, after the second LPF block, HESS power can be divided into parts: battery power $P_{bat,ref}$ and SC power $P_{SC,ref}$. It should be noted that the initial battery and SC power distribution may exceed the power limits and SoC limits. Then, the EMS block regulates the battery and SC power again and feedback to the input power to ensure the battery and SC work within prescribed power and SoC limits. The feedback coefficients are related to the state of energy and power level of the battery and SC. Note that the EMS operation is also smoothed by the RR control block to guarantee the power fluctuations of the grid-connected power P_{grid} within limits.

In this paper, the cutoff frequencies of two LPF blocks f_{c1} and f_{c2} are adjusted based on two APF algorithms, respectively. The two APF algorithms are named RR-APF and SoC-APF, which will be demonstrated in detail in the next section.

2.2. System model

2.2.1. PV model

This paper adopts the power temperature coefficient model, based on [31], to represent the PV module and the PV power at maximum power point (MPP). These can be expressed as:

$$P_{mp}(G_e, T_c) = \frac{G_e}{G_{STC}} P_{mp,STC}\left[1 + \gamma_{mp}(T_c - T_{STC})\right] \tag{1}$$

$$T_c = T_{amb} + (NOCT - 20)\cdot\frac{G_e}{800} \tag{2}$$

where G_e is effective in-plane solar irradiance and G_{STC} is the solar irradiance under the standard test condition (STC). $P_{mp,STC}$ and γ_{mp} are the measured peak power under STC and the normalized temperature coefficient of peak power, respectively. T_c, T_{amb}, and T_{STC} are, respectively, the solar cell temperature, ambient temperature, and the temperature at STC conditions. *NOCT* is the normal operating cell temperature.

2.2.2. Battery degradation model

In order to evaluate the effect of the current rate and energy throughput on battery lifetime, a Li-ion battery degradation model is used in this study [32]. This model is semi-empirical, and the parameter is calibrated through experiment tests in [33]. The total loss Q_{loss} during a period and instantaneous battery degradation $\Delta Q_{loss}(k)$ after discretization can be expressed as:

$$Q_{loss} = 0.0032e^{\left(\frac{-15162+1516C_{rate}}{R(|T_b - T_{bat}| + T_C)}\right)} \cdot A_h^{0.849} \tag{3}$$

$$\Delta Q_{loss}(k) = \Delta A_h z B^{\frac{1}{z}} e^{-\left(\frac{E_a + C\cdot C_{rate}}{zR(|T_b - T_{bat}| + T_C)}\right)} Q_{loss}(k-1)^{\frac{z-1}{z}} \tag{4}$$

In (3) and (4), C_{rate} and C are the battery discharge rate and the

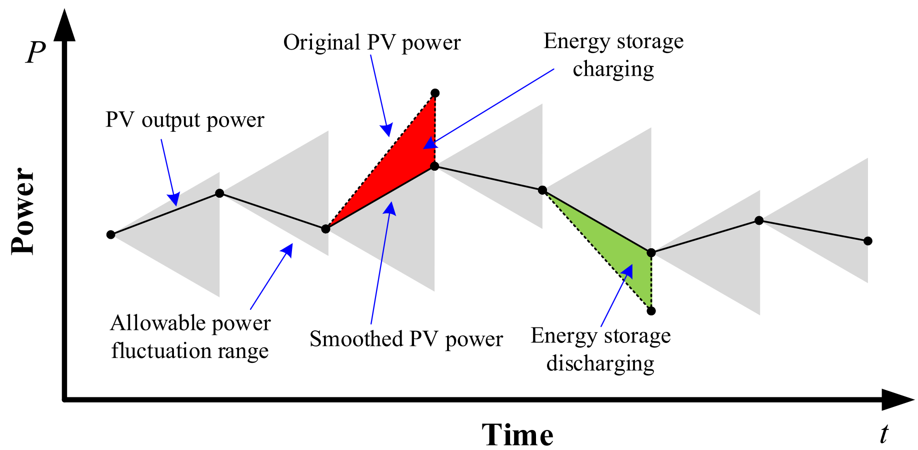

Fig. 3. Principle of power RR limit.

compensation factor of C_{rate}, respectively. T_{b}, T_{bat} and T_{C} are the baseline temperature, work temperature, and compensation temperature, respectively, which are all measured in Kelvin temperature (K). Q_{loss} is the percentage of battery capacity loss. k is the k-th time instant and ΔA_{h} is the Ah-throughput during this instant. z is the time factor and R is the gas constant (J/molK). E_{a} is the activation energy (J).

The battery SoC and its limitation can be expressed as:

$$SoC_{bat}(t) = SoC_{bat}(t-1) - \frac{\eta_{ch}}{E_{bat}}(P_{cha}(t)\cdot\Delta t) + \frac{1}{\eta_{disch}\cdot E_{bat}}(P_{discha}(t)\cdot\Delta t) \quad (5)$$

$$SoC_{bat\_\min} \leqslant SoC_{bat}(t) \leqslant SoC_{\text{bat\_max}} \quad (6)$$

$$-P_{\text{bat\_max}} \leqslant P_{bat}(t) \leqslant P_{\text{bat\_max}} \quad (7)$$

where $SoC_{bat}(t)$ and $SoC_{bat}(t\text{-}1)$ are the battery SoC at t and t-1 moment, respectively. Δt is the time interval and E_{bat} is the battery's nominal capacity. η_{ch} and η_{discha} are the charging and discharging efficiency, and P_{cha} and P_{disch} are the charging and discharging power, respectively. $SoC_{\text{bat min}}$ and $SoC_{\text{bat max}}$ are battery minimum and maximum SoC, respectively. And $P_{\text{bat max}}$ is the maximum allowable power of the battery.

2.2.3. SC model

Considering the long lifespan of SC, the SC cycle model is employed is this paper, which is expressed as:

$$SoC_{SC}(t) = SoC_{SC}(t-1) - \frac{\eta_{ch}}{E_{SC}}(P_{cha}(t)\cdot\Delta t) + \frac{1}{\eta_{disch}\cdot E_{SC}}(P_{discha}(t)\cdot\Delta t) \quad (8)$$

$$SoC_{SC\_\min} \leqslant SoC_{SC}(t) \leqslant S0C_{\text{SC\_max}} \quad (9)$$

$$-P_{\text{SC\_max}} \leqslant P_{SC}(t) \leqslant P_{\text{SC\_max}} \quad (10)$$

where $SoC_{SC}(t)$ and $SOC_{SC}(t\text{-}1)$ are the battery SoC at t and t-1 moment, respectively. Δt is the time interval and E_{SC} is the nominal capacity of SC. η_{ch} and η_{discha} are the charging and discharging efficiency, and P_{cha} and P_{disch} are the charging and discharging power, respectively. $SoC_{\text{SC min}}$ and $SoC_{\text{SC max}}$ are the battery minimum and maximum SoC, respectively, while $P_{\text{SC max}}$ is the maximum allowable power of the SC.

3. Proposed power smoothing approach

In this section, the PV power fluctuation is first defined. Then, the artificial potential field method is introduced to act as a frequency decomposition method. Considering the characters of power RR and the storage SoC, we use an asymmetric APF-based LPF to decompose the PV power and limit the RR of grid-feeding power, and use a symmetric APF-based LPF to allocate power between the battery and SC. By regulating the parameters of APF, the cut-off frequency of LPF can be adjusted accordingly. As a result, the PV power RR can be controlled within prescribed limits, and the battery and SC can operate within a proper SoC range.

3.1. Definition of power ramp rate

Power ramp rate $RR(t)$ is defined as the power difference between the present value $P(t)$ and the previous sampling time power $P(t\text{-}\Delta t)$, normalized to the rated PV capacity P_{rated} of the plant, which can be expressed as:

$$RR(t) = \frac{P_{PV}(t) - P_{PV}(t-\Delta t)}{P_{rated}} \times 100\% \quad (11)$$

In this paper, a limit of 10 %/min is adopted, i.e., PV output power fluctuation cannot exceed 10 % of its capacity within one arbitrary minute [5]. The principle of power RR limit is shown in Fig. 3. The black line is the output power of the PV plant, and the brown triangular blocks are the prescribed power range. If the original PV power increases fast and is over the range, HESS needs to absorb excess energy (i.e., red triangle part) to limit the power RR. On the other hand, when the original PV power decreases too fast, HESS needs to release energy (i.e., the green triangle part) if PV power is below the range. Hence, the RR of the smoothed grid-connected power can be ensured within 10 %/min.

3.2. Establishment of the artificial potential field

The APF method is originally proposed in path planning and autopilot applications [34,35], which is also reported in electrical vehicle cases recently [36,37]. It is assumed that there is no force between two objects when the distance is x_{ref}. When the distance is larger than x_{ref}, there is an attractive force, and when the distance is smaller than x_{ref}, there is a repulsive force between them. The further away from this point x_{ref}, the greater the attractive/repulsive force between the two objects.

In this paper, we use power RR and battery SoC to map the distance, respectively. And two APF-based LPFs are used to distribute power among the grid, battery and SC.

3.2.1. Asymmetric APF for RR control

In real applications, PV power can fluctuate within a wide range, which can be up to 90 % [38]. Considering the prescribed RR limit is 10 %/min, we set $RR_{\min}$ and $RR_{\max}$ are 10 % and 90 %, respectively. RR below 10 % is not filtered, while RR above 90 % is filtered with the greatest force. Due to the delay effect of LPF, we set the RR baseline

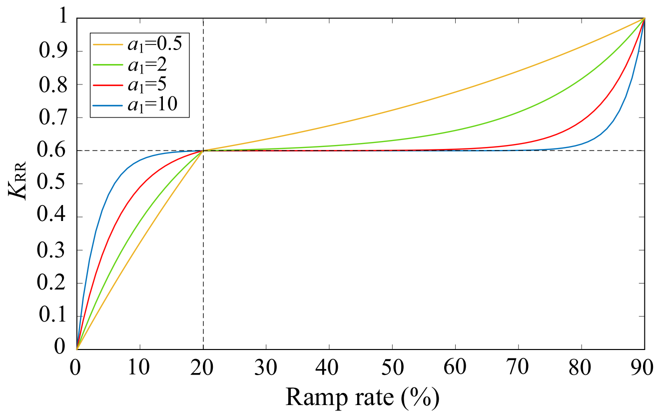

Fig. 4. Relationship between normalized virtual force K_{RR} and power ramp rate.

equal to 20 %, i.e., $RR_{ref} = 20$ %.

The virtual force F_{RR} regarding RR can be represented as:

$$F_{RR} = \begin{cases} \dfrac{20^{|a_1 x_1|} - 1}{20^{|a_1 (RR_{max} - RR_{ref})|} - 1} & x_1 \geqslant 0 \\ \dfrac{20^{|a_1 x_1|} - 1}{20^{|a_1 (RR_{ref} - RR_{min})|} - 1} & x_1 < 0 \end{cases} \tag{12}$$

In (9), $x_1 = RR\text{-}RR_{ref}$, which represents the distance to the preset point. a_1 is a coefficient to shape the curve of the virtual force F_{RR}. In the ramp rate application, the virtual attractive force needs to be normalized to [0,1] during frequency decomposition. As a result, K_{RR} is introduced, which is given below:

$$K_{RR} = \left[0.5 + sign(-F_{RR})\cdot\left(K_{RR\_ref} - 0.5\right)\right]\cdot F_{RR} + K_{RR\_ref} \tag{13}$$

where K_{RR_ref} is the set point of K_{RR}. A higher K_{RR_ref} means a higher tolerance for high power fluctuations.

Fig. 4 shows the relationship between normalized virtual force K_{RR} and the power RR with different a_1 values. It can be seen that the exponential characteristic of the curve is more pronounced when a_1 is increasing.

Fig. 5 shows an illustration of cutoff frequency adjusting of LPF for RR control. Firstly, a vector consisting of N_1 points of PV power is through a fast Fourier transform (FFT) block and gets a frequency spectrum. Meanwhile, according to the PV power RR value at the present moment, the normalized virtual attractive/repulsive force K_{RR} can be calculated according to (13). Then, the area equal to K_{RR} of the high-frequency portion in the spectrum is undertaken by the HESS, and the low-frequency portion equal to 1-K_{RR} is fed into the grid. Therefore, once K_{RR} is determined, the cutoff frequency of the LPF can be determined. According to different values of power RR, the cutoff frequency of LPF can be adjusted dynamically, thereby ensuring smoother power within the prescribed range.

3.2.2. Symmetric APF for HESS power allocation

In order to reduce battery stress and extend its lifetime, a symmetric APF-based LPF is used to allocate power between the battery and SC dynamically. In this paper, the battery SoC is used to regulate the virtual force, which helps to make the battery SoC approach the reference value, where the operational range of battery SoC is [0.1, 0.9]. Therefore, the following limits are set: $SoC_{mid} = 0.5$, SoC_{min} and SoC_{max} are 0.1 and 0.9, respectively. the virtual force F_{HESS} for SoC control can be expressed as:

$$F_{HESS} = -sign(P_{HESS})\cdot sign(x_2)\cdot\frac{20^{|a_2 x_2|} - 1}{2\left(20^{0.4a_2} - 1\right)} \tag{14}$$

where $x_2 = SoC_{bat}$ - SoC_{mid}, and 0.4 is the value of SoC_{mid} - SoC_{min} and SoC_{max} - SoC_{mid}. P_{HESS} is the HESS power, and the virtual force curve is opposite when HESS is charging and discharging. a_2 is the curve coefficient of the virtual force.

Similarly, K_{HESS} is introduced to normalize the virtual force F_{HESS} during HESS power distribution, which is expressed as:

$$K_{HESS} = F_{HESS} + 0.5 \tag{15}$$

Fig. 6 shows the relationship between the normalized virtual force K_{RR} and the battery SoC with $a_2 = 0.5$, 1.5, 3, 5, and 8 respectively. The solid lines represent the battery discharging cases while the dash lines represent the charging cases. It is noted that the directions of the normalized virtual force K_{HESS} are opposite in charging and discharging cases. Specifically, with the increasing a_2, the exponential characteristics of K_{HESS} are more pronounced. As a result, when the battery SoC is approaching its upper limit, less charging power or more discharging is

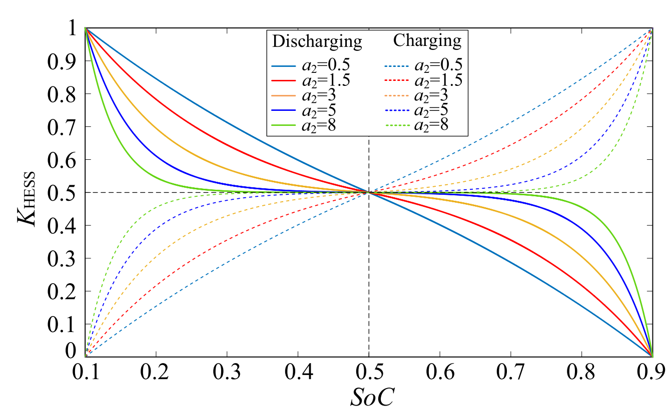

Fig. 6. Relationship between normalized virtual force K_{HESS} and battery SoC.

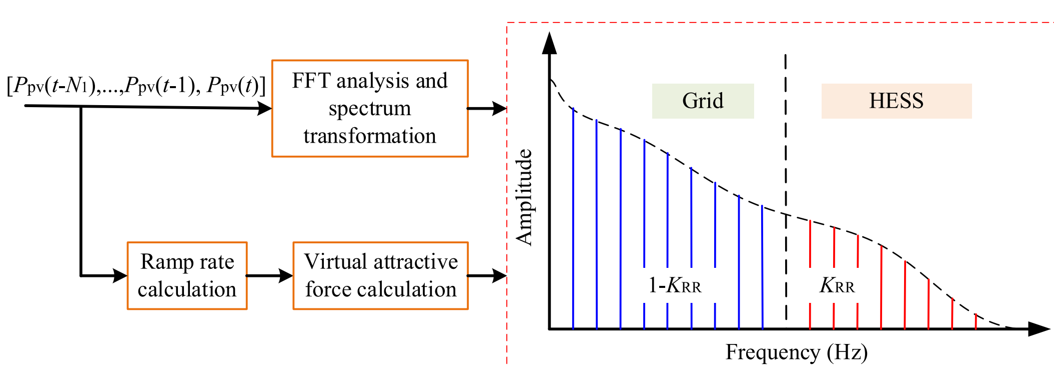

Fig. 5. Principle of cutoff frequency adjusting of RR-APF.

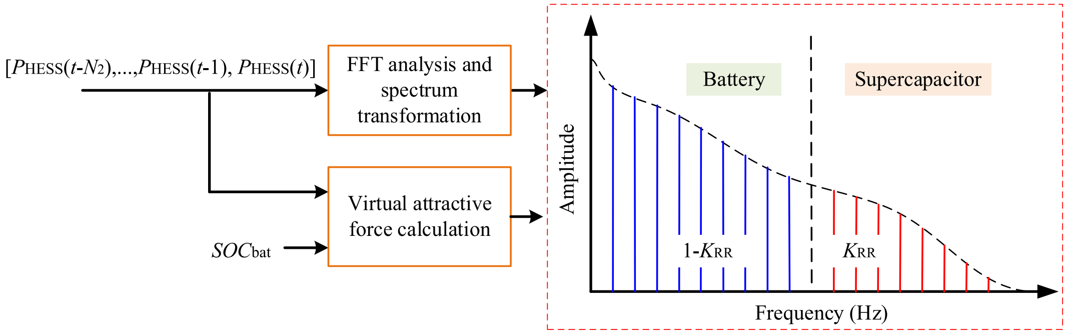

Fig. 7. Principle of cutoff frequency adjusting of SoC-APF.

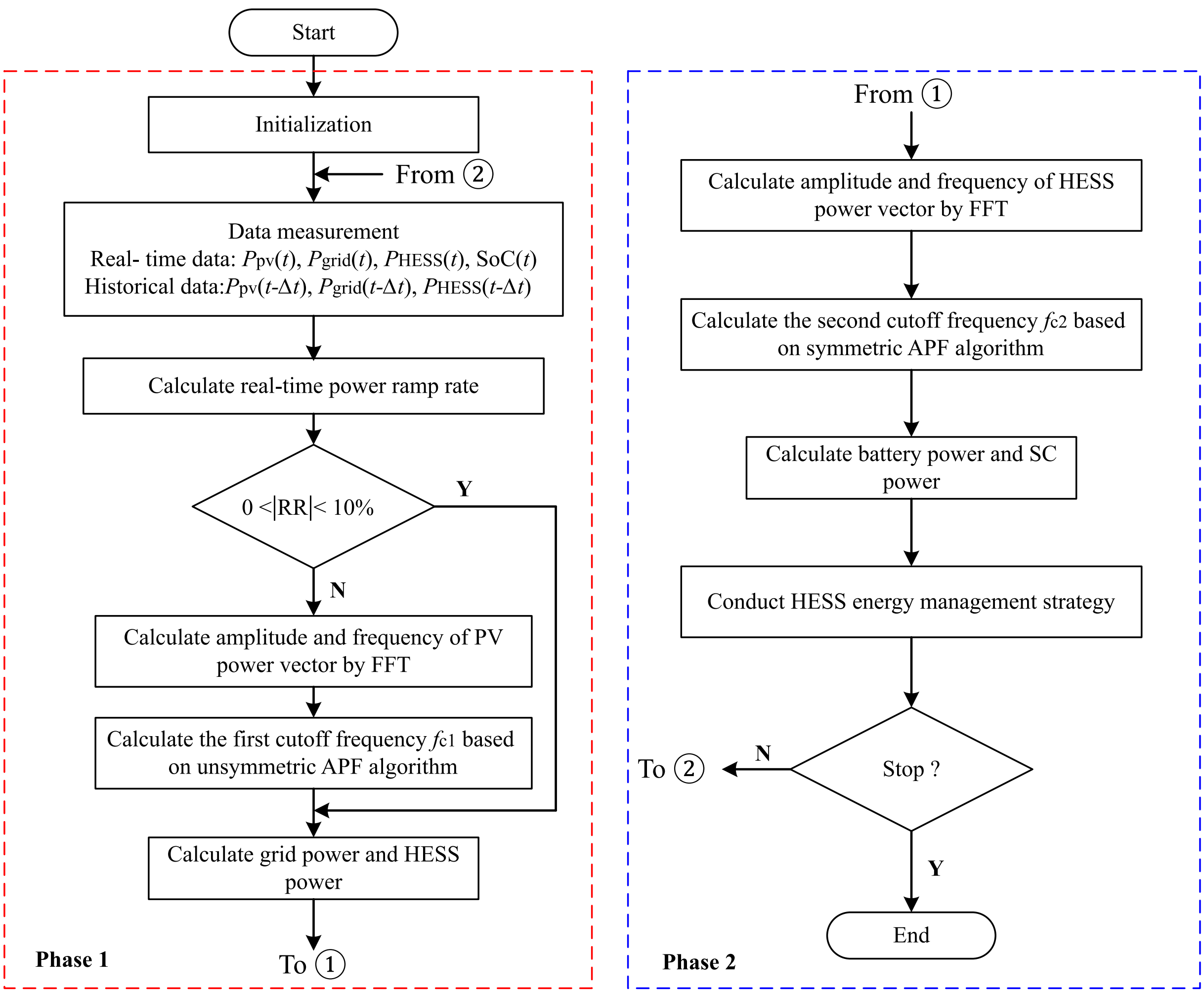

Fig. 8. Flowchart of the proposed frequency decomposition approach.

undertaken by the battery, and vice versa. Hence, the battery stress can be reduced to some degree.

Fig. 7 shows an illustration of the cutoff frequency adjusting of LPF for HESS power distribution. Similarly, a vector of HESS power consisting of N_2 points is decomposed through the FFT algorithm and gets a frequency spectrum. Meanwhile, K_{HESS} can be calculated according to Eq. (12). Then, the battery and SC get the power signals respectively, which are equal to K_{HESS} and 1- K_{HESS} of P_{HESS}. As a consequence, the cutoff frequency can be determined and adjusted dynamically.

3.3. *Strategy implementation*

Fig. 8 shows the flowchart of the proposed strategy based on APF, which consists of two phases: RR control and HESS power allocation. The steps of this strategy are as follows:

Step 1: Initialize each variable.

Step 2: Measure the PV and grid real-time power, battery and SC SoC, and historical data of P_{pv} and P_{grid}.

Step 3: Calculate the real-time power fluctuation of P_{pv} and P_{grid}. If the power RR meets the prescribed limit, the original PV power is directly connected to the grid. Otherwise, perform the APF algorithm,

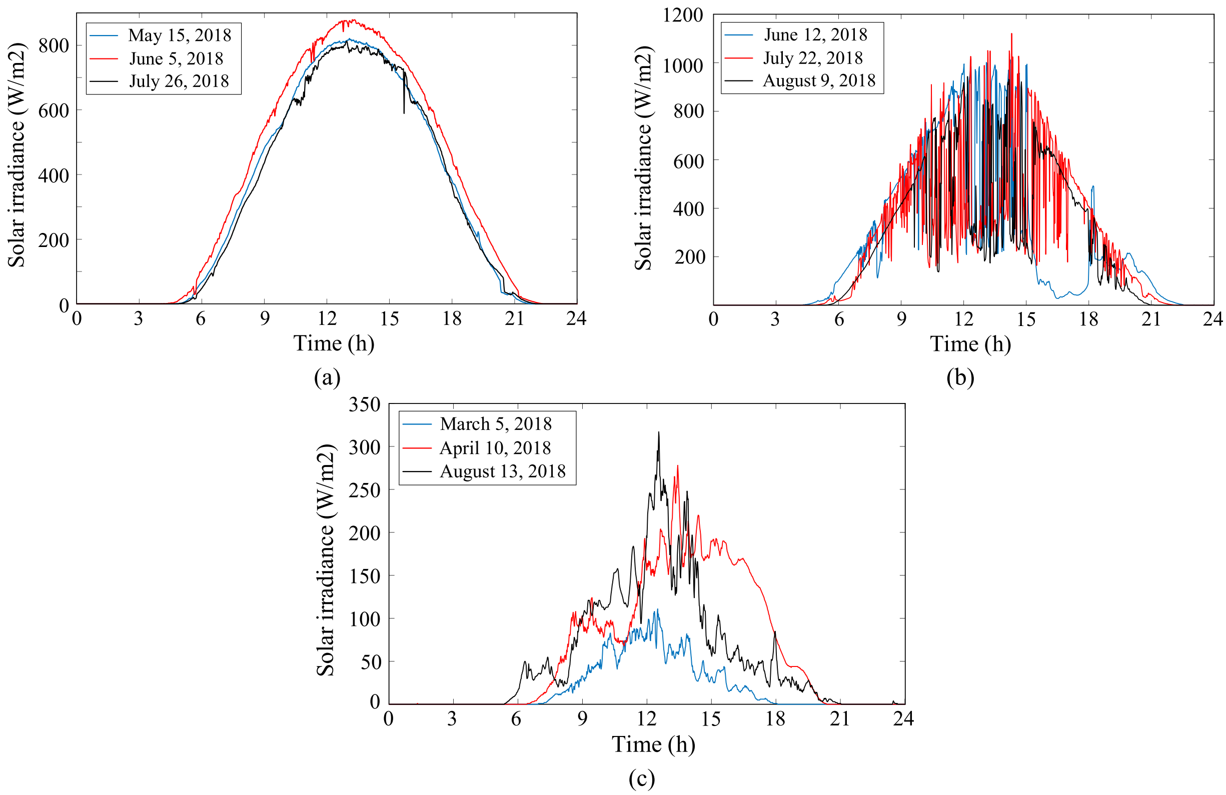

Fig. 9. Typical scenarios of PV irradiance; (a) sunny; (b) partly-cloudy; (c) overcast.

Table 2
Simulation parameters for PV-HESS system.

Description	Parameter	Value
Rated PV capacity	P_{rate}	1.5 MW
Battery energy capacity	E_{bat_rated}	150 kWh
Battery power capacity	P_{bat_rated}	300 kW
SC energy capacity	E_{SC_rated}	50 kWh
SC power capacity	P_{SC_rated}	500 kW
Battery maximum SoC	SoC_{bat_max}	0.9
Battery minimum SoC	SoC_{bat_min}	0.1
SC maximum SoC	SoC_{SC_max}	0.85
SC minimum SoC	SoC_{SC_min}	0.15
SoC feedback coefficient	K_{feed}	0.5

and calculate the power demand of HESS power P_{HESS}.

Step 4: According to the power demand of HESS, perform the APF algorithm to calculate the cutoff frequency of LPF to distribute power between the battery and SC.

Step 5: Apply the energy management strategy of HESS to ensure the battery and SC operate within power and SoC limits.

Step 6: Determine if the loop has ended. If not, update the measured data and wait for the next calculation.

4. Case study

This section takes the real operation data of a weather station in Denmark as an example to validate the effectiveness of the proposed strategy on RR control and extending battery lifetime. During this process, three strategies for power smoothing, i.e., LPF, MA, and varying TC-based strategy [21], are chosen as comparisons.

4.1. Data and simulation parameters

According to the fractal classification algorithm [39], the weather can be divided into three categories: sunny, partly-cloudy, and overcast. Fig. 9 shows some typical days of the three scenarios, which can reflect the general characteristics of PV power fluctuations. The data are measured with a sampling interval of 1 min. Due to the size limitation, only three typical days are shown in every scenario.

Before simulation, the system parameters and configuration should be demonstrated. In this paper, the RR limit is set to 10 %/min for both upward and downward limitation. The PV station is in Denmark with 1.5 MW rated capacity. The HESS comprises of a 150 kWh Li-ion battery and 50 kWh SC, and their power capacity are 300 kW and 500 kW, respectively. The battery and SC SoC operation ranges are [0.1, 0.9] and [0.15, 0.85] [22], respective. Table 2 list the simulation parameters used to evaluate the proposed strategy for the PV-HESS system.

4.2. Parameter design and analysis

4.2.1. Determination of sampling points N_1 and N_2

Among the three types of weather conditions, partly-cloudy days will lead to the most power fluctuations. Therefore, in order to achieve an effective power decomposition under various weather conditions, a typical partly-cloudy day July 22 in Fig. 9(b) is chosen to design the parameters of the proposed power smoothing approach.

The number of sampling points directly determines the level of filter TCs, which needs to be designed firstly. Generally speaking, more sampling points can provide more tuning steps for TC, yet reflect fewer characteristics of current power signals. Therefore, the aim of designing the numbers of sampling points N_1 and N_2 is to provide enough changing steps and reduce the "memory effect" of the proposed approach. Fig. 10 shows the TCs of two LPFs with different numbers of sampling points. It should be noted that the left side and the right side are the TC of LPF1 and LPF, respectively, which are represented with * and °, respectively.

Fig. 10(a) shows that when the sampling points $N_1 = N_2 = 10$, the tuning steps of two TCs of LPFs are both 5, which means that the 10 sampling points cannot provide enough steps to decompose the PV

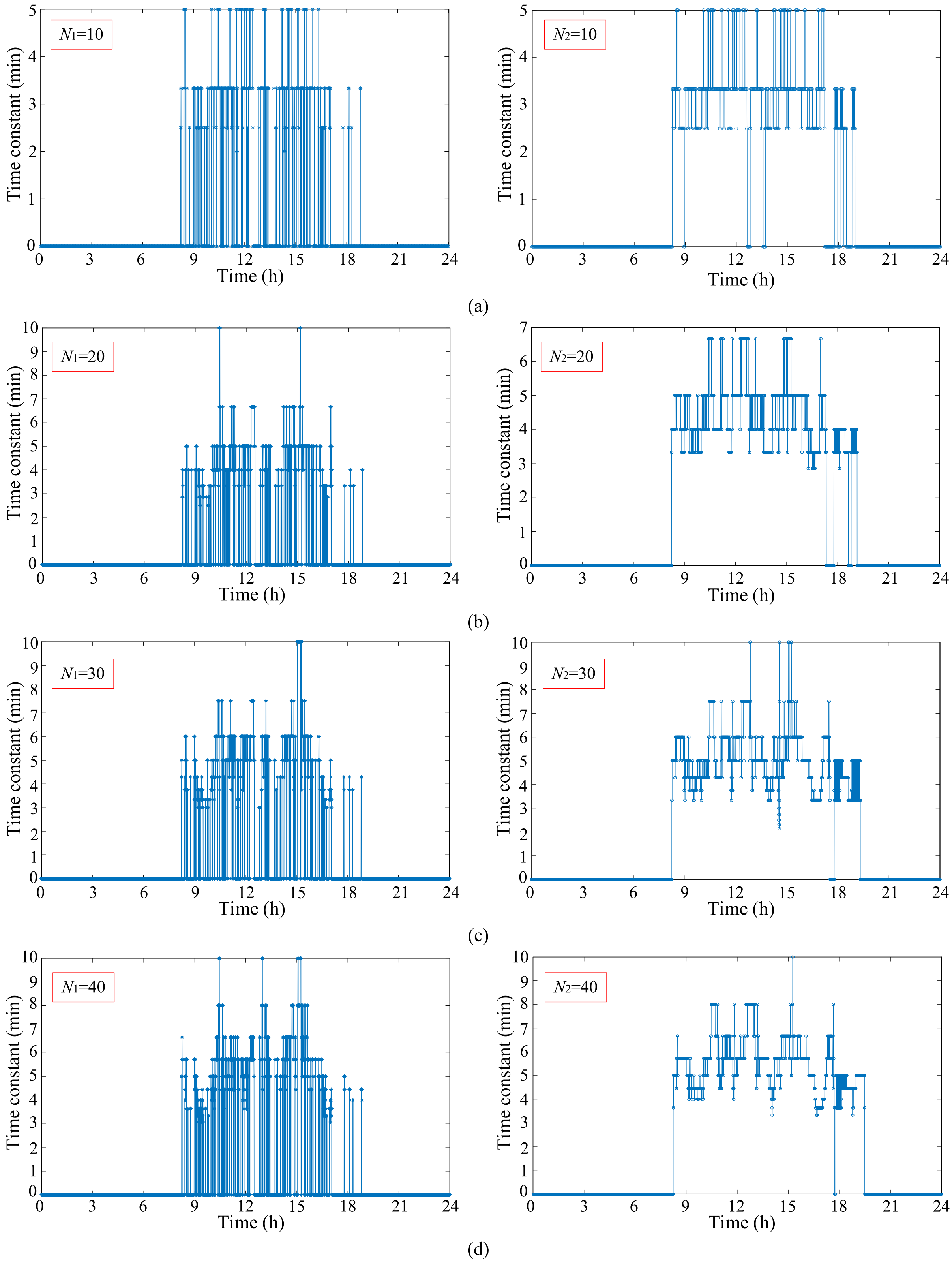

Fig. 10. TCs of two LPFs under different number of sampling points; left: TC of LPF1; right: TC of LPF2.

power and HESS power. When $N_1 = N_2 = 20$, as shown in Fig. 10(b), the TCs of LPF1 and LPF2 are within 7 min in most time of the day, and the TC of LPF1 can reach to 10 min only in some high PV RR cases. Furthermore, when increase the sampling points, as shown in Fig. 10(c)(d), the TCs of LPF1 and LPF2 can only reach 10 min, which means 10 tuning steps are enough for the TC of two LPFs. Therefore, the number of sampling points are designed as $N_1 = N_2 = 20$.

4.2.2. Determination of curve coefficient a_1 and a_2

The coefficient a determines the curve shapes of the virtual force to influence the cutoff frequency of LPF, which has the most important impacts on the results of frequency decomposition. In the design process,

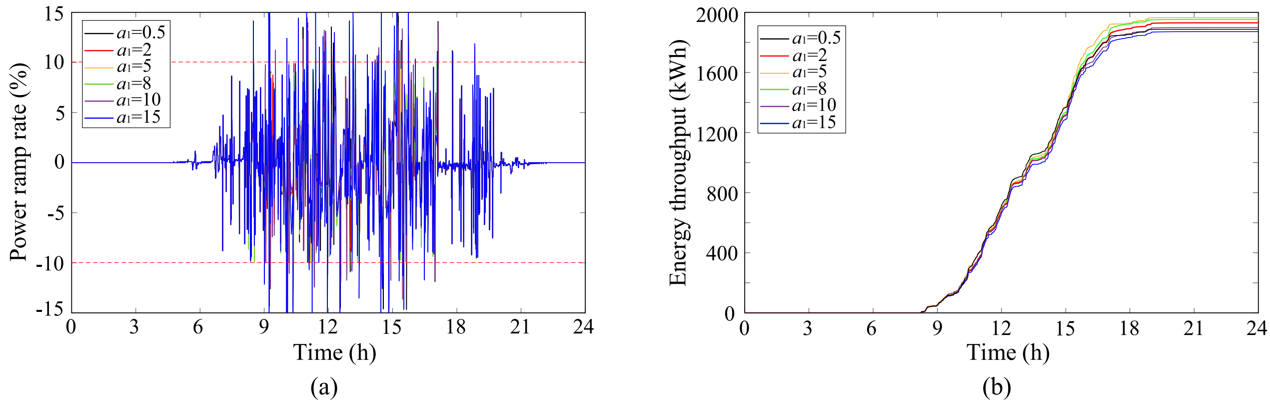

Fig. 11. Smoothed power ramp rate and energy throughput of HESS under different a_1 parameters; (a) power ramp rate; (b) energy throughput of HESS.

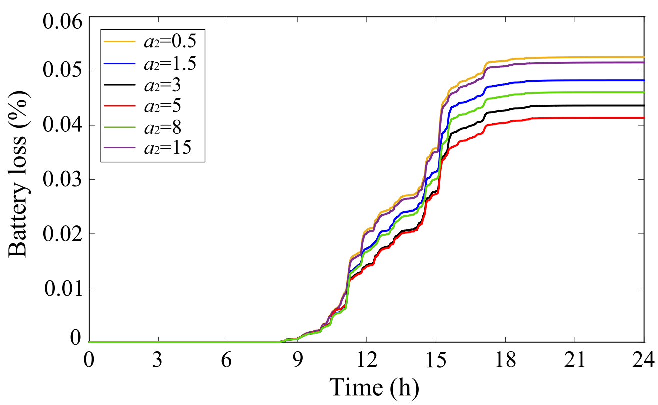

Fig. 12. Battery capacity loss under different a_2 parameters.

the coefficient a_2 for the SoC-APF is fixed as 1, then study the smoothing effects with different a_1 for RR-APF. In this regard, six a_1 values, i.e., $a_1 = 0.5$, 2, 5, 8, 10, 15, respectively are tested, and the RR of smoothed power and energy throughput of HESS are shown in Fig. 11. It can be seen from Fig. 11(a) that some a_1 values will make the RR of smoothed power exceed 10 %/min, which means the a_1 has a value range to guarantee the RR within the prescribed limit. Specifically, when $a_1 = 0.5$ or greater than 10, the RR of smoothed power exceed 10 %/min, and the maximum RR under $a_1 = 15$ is lower than that under $a_1 = 10$. That says, when a_1 is less than 0.5 or greater than 10, the RR limit cannot be met anymore. On the other hand, when $a_1 = 2$, 5 and 8, the RR of smoothed power are both below 10 %/min. Furthermore, the power RR is lower under $a_1 = 5$ and 8 than that under $a_1 = 2$, which will smooth out more high-frequency power.

Fig. 11(b) shows the energy throughput of HESS with different a_1 values, which calculates the amount energy (measured in absolute value) smoothed out under the six cases. The energy throughput with $a_1 = 0.5$, 2, 5, 8, 10, and 15 are 1871kWh, 1930kWh, 1953kWh, 1950kWh, 1883kWh, and 1868kWh, respectively, which accords with the smoothing results in Fig. 9(a). However, more energy throughput of HESS means more battery and SC use, which will reduce their lifespans. Therefore, considering the RR requirement and energy throughput of HESS (i.e., battery use), $a_1 = 2$ is selected for the RR-APF.

After determining the coefficient a_1 for RR control, a_2 can be designed to distribute the power between the battery and SC to reduce the battery degradation. In this process, a_1 is fixed as 2, which is designed above, and then change a_2 to compare the battery capacity loss under different a_2 cases.

Fig. 12 shows the percentage of battery capacity loss under different a_2 values with the same PV profile as Section 4.2.1. It can be seen that when a_2 increases, the battery loss decreases in the beginning and then increases again. Specifically, when a_2 increases from 0.5 to 5, the battery loss decreases from 0.053 % to 0.042 %. And when a_2 increases to 15, the battery loss increases to 0.051 %, which means the battery can obtain the least degradation when $a_2 = 5$. Therefore, in order to achieve a better battery degradation performance, $a_2 = 5$ is selected for SoC-APF.

4.3. Performance assessment of proposed approach

After designing the parameters, the performance of the proposed approach can be assessed. Fig. 13 shows the power smoothing and allocation results. It can be seen from Fig. 13(a) and Fig. 13(b), the grey curve is the original PV power, and the red curve is smoothed power to the grid. After the suppression, the RR of grid-connected power is reduced significantly, which meet the prescribed 10 %/min standard. Moreover, the proposed strategy doesn't smooth out the PV power with below 10 %/min RR, which reduces the over-smoothing operation. Hence, the energy throughput and capacity of HESS can be reduced. Fig. 13(c) and Fig. 13(d) show the TCs of LPF1and LPF2, respectively. When conducting the FFT analysis, the number of frequency components in the frequency spectrum is equal to a half of the number of vector elements. In this section, the number of measured points of PV power and HESS power are both 20, which can provide enough TC levels. In Fig. 13(c), when the power fluctuations are below 10 %, the TC of first LPF is 0, which means all energy flows to the grid without smoothing and no energy flows to the HESS. In Fig. 13(d), TC has more regulation levels for HESS power distribution than that in RR control. This is because the battery SoC varies slowly and has same effect on both sides of the SoC reference due to the symmetric APF. Then, the second APF-LPF decomposes the HESS power into high-frequency and intermediate-frequency components and allocate power between the battery and SC dynamically.

It can be seen from Fig. 13(e)(f) that the SC undertakes the power with high fluctuations and the battery provides a slow power compensation. Initially, the battery and SC SoC are both 50 %. After one day of operation, the battery and SC SoC return to their initial value, which means that the SoC control can ensure the battery and SC operate within prescribed ranges and all power is released to support the RR control operation. As a result, the battery and SC do not need to charge/discharge additionally at the end of the day.

4.4. Performance comparison with existing strategies

4.4.1. Comparison of the smoothing effect in case of different strategies

Generally speaking, for the LPF-based and MA-based power smoothing techniques, the larger TC or time window, the better smoothing effect can be obtained. However, the energy storage has limitations of power capacity and energy capacity, which constraint the ranges of TC and time window. Besides, one aim of this study is to reduce

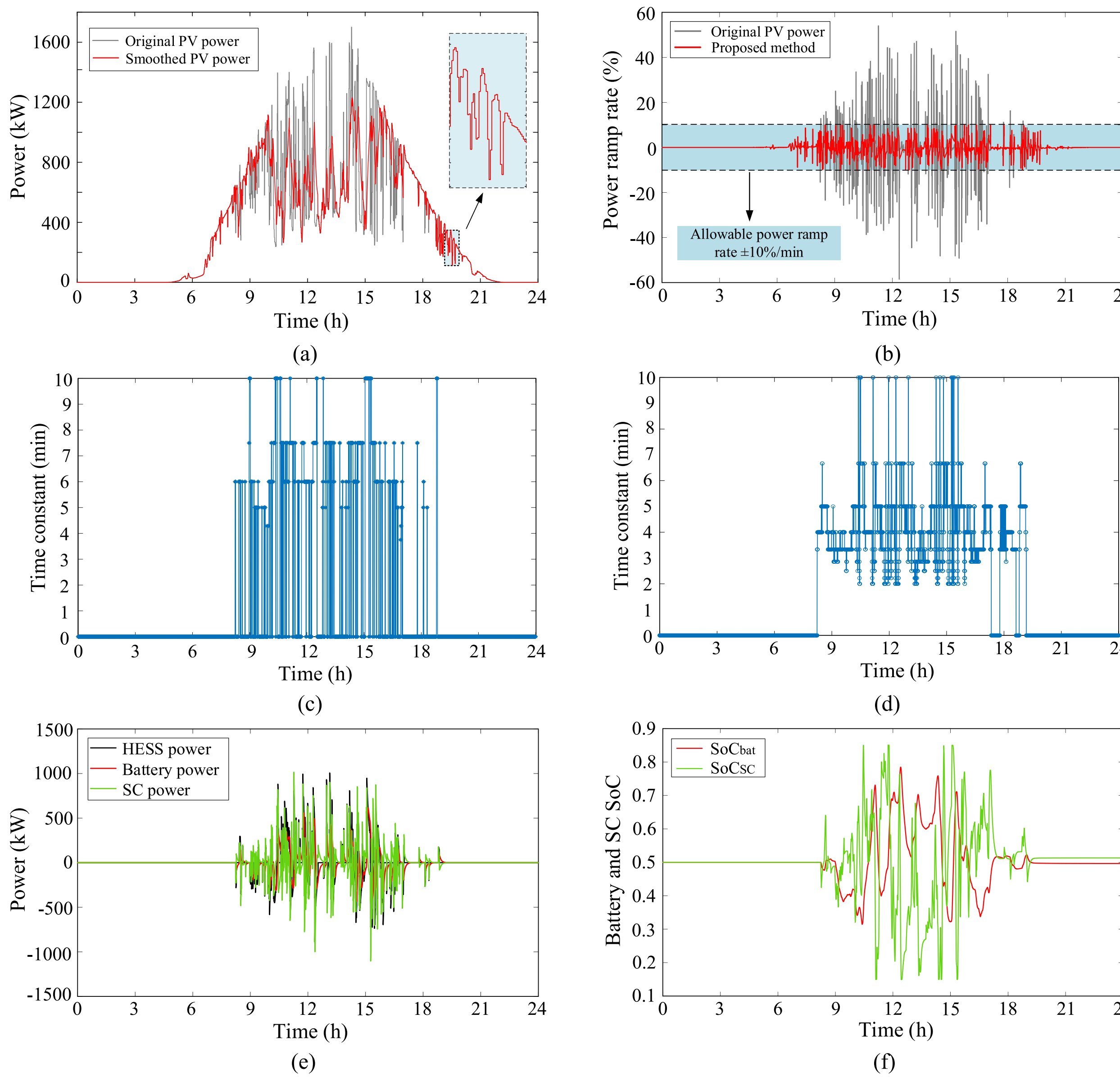

Fig. 13. Adaptive smoothing on a partly-cloudy day; (a) PV power comparison; (b) ramp rate comparison; (c) TC of LPF1; (d) TC of LPF2; (e) HESS, battery and SC power; (f) SoC of battery and SC.

the energy storage capacity, thus increasing the TC value or time window is not practical. In this study, the dataset of July 22 in Fig. 9(b) is taken as an example. For the fixed TC LPF-based strategy, the TC values of two LPF are set to 6 min and 2 min, respectively, and the time window is set to 10 min for the fixed MA-based strategy. For the varying TC-based strategy, the initial TC value is 5 min. For the proposed approach, the sampling points $N_1$and N_2 are both 20 min, and curve coefficients a_1 and a_2 are set to 2 and 5, respectively.

Fig. 14 shows the smoothing results of different methods. In terms of RR control effect, each method can meet the prescribed limit 10 %/min, but the proposed strategy outperforms the other smoothing methods in power phase lagging and energy throughput of HESS. This is because the proposed strategy can regulate the TC dynamically and will not smooth the "compliant" power (i.e., RR below 10 %/min), as shown in Fig. 14 (a). In contrast, the fixed value smoothing methods of LPF and MA smooth the power consecutively in a preset manner, which can get the best smoothing effect in the cost of over-smoothing and power phase lagging, as shown in Fig. 14(a) and Fig. 14(b). Additionally, in the case of the varying TC strategy, the phase lagging can be reduced to some degree, but the "compliant" power is still smoothed out, as presented in Fig. 14(a). Fig. 14(c) shows the energy throughput of HESS under different smoothing approaches. The total energy throughput of LPF, MA, varying TC method, and the proposed method are 2139 kWh, 2083 kWh, 2047 kWh, and 1859 kWh, respectively. As a result, the reduction in HESS energy throughput makes energy storage reduction and battery lifetime extension a possible benefit.

4.4.2. Battery degradation comparison

In (4), the instantaneous battery capacity loss is relevant to its previous value. Here, we assume the initial battery capacity loss is 1 %, and then calculate the battery loss increment in the case of the chosen typical day. Fig. 15 shows the battery and SC SoC and the battery degradation result, where the initial SoC of the battery and SC are both 0.5.

As can be observed from Fig. 15(a) and Fig. 15(b), the SoC of battery and SC under different methods operate within the preset ranges, and the final SoC can return to their initial values. Besides, from the battery SoC, it can be seen that the MA method has the minimum SoC variation range while the proposed method has the maximum SoC variation

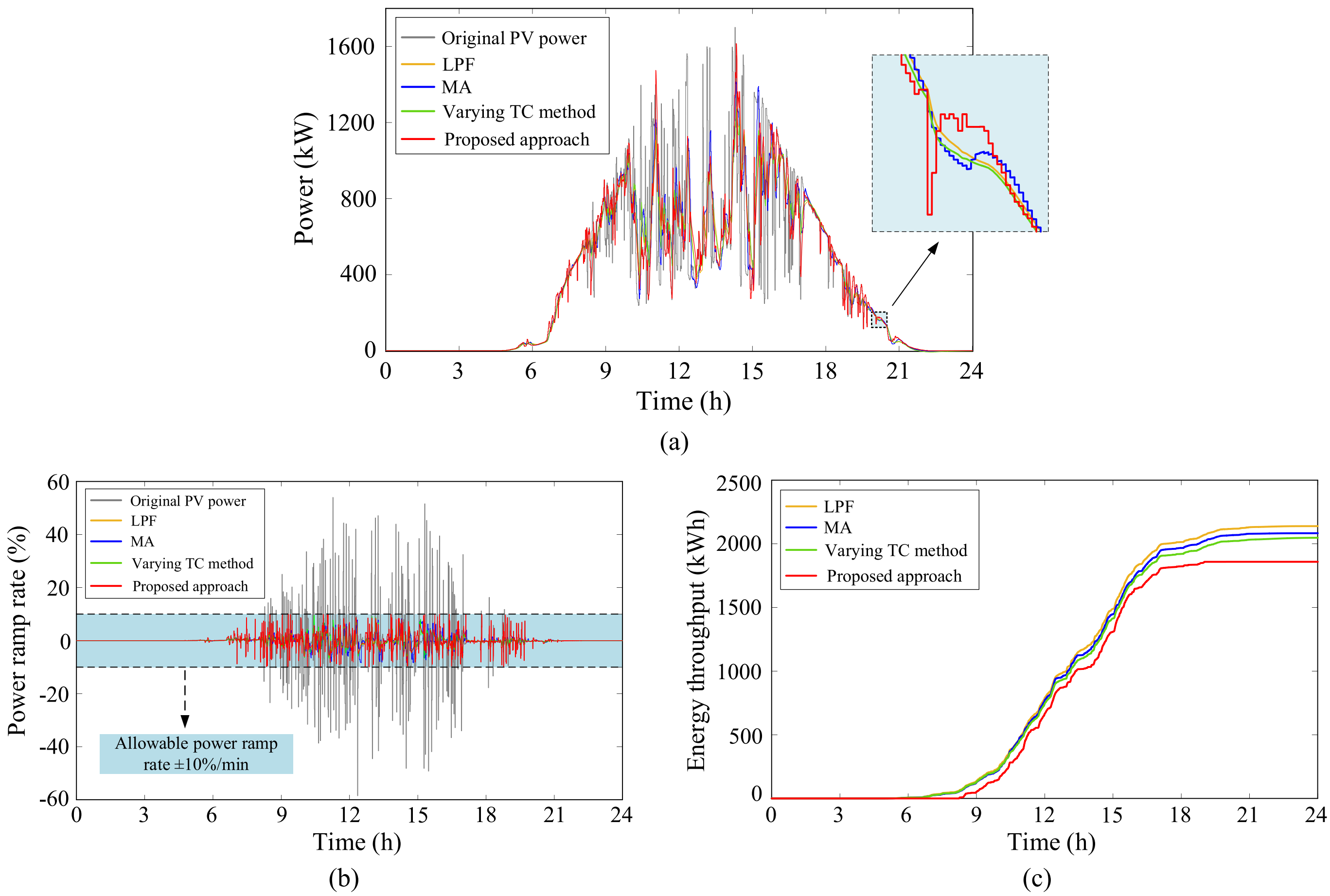

Fig. 14. Comparison of smoothing effect of different strategies; (a) smoothing profile; (b) power ramp rate; (c) energy throughput of HESS.

range. This is because the SoC control makes the battery SoC tends to return to its reference SoC, and more energy throughput will occur in the case of SoC control. Though applying the SoC control as well, the proposed method is based on the virtual attractive force (i.e., artificial potential field), and the battery reference power will change automatically when the SoC deviates from its reference value. As a result, the SoC control has less effect in the case of the proposed method, thus reducing the battery stress.

Fig. 15(c) shows the battery capacity loss under different smoothing methods. It can be seen that the MA with fixed time window has the most battery degradation, while the proposed method has the best performance in battery degradation, which is consistent with the battery SoC trend in Fig. 15(a). The battery degradation in the case of LPF, MA, varying TC-based method, and the proposed method are 0.066 %, 0.083 %, 0.051 %, and 0.042 %, respectively. In other words, the proposed smoothing strategy can reduce battery capacity loss by 36.4 %, 49.4 %, and 17.6 % compared to LPF, MA, and the varying TC-based method. Therefore, the obtained results illustrate the proposed smoothing strategy has superior performance in extending the battery lifetime.

5. Conclusion

This paper proposes a novel power smoothing approach for a PV plant with the battery-supercapacitor system to reduce PV power uncertainty. The proposed approach uses a two-stage adaptive time constant low-pass filter based on the artificial potential field to decompose and allocate the PV power. In the ramp rate control stage, the proposed strategy adopts an unsymmetric APF to change the cutoff frequency of a low-pass filter, which reduces the "over smoothing" effect meanwhile ensures the grid-connected power within the prescribed limit. In the HESS power distribution stage, the proposed approach adopts a symmetric APF to allocate power and gives the full play to the advantages of HESS.

Compared with other alternative smoothing methods in PV applications in the cases of HESS, case study proves that the proposed approach outperforms in some respects. Firstly, the proposed method doesn't rely on weather prediction and can ensure real-time control. Secondly, less energy throughput of HESS for the proposed method, which can reduce storage capacity and cycles. In addition, the proposed approach has a lower battery degradation, which can reduce battery capacity loss by 36.4 %, 49.4 %, and 17.6 % compared to LPF, MA, and the varying TC-based method, respectively.

The proposed frequency decomposition-based smoothing method considers the past and present data to conduct FFT analysis and frequency decomposition. In the future, adopting the prediction algorithm and applying the future data can be further explored.

CRediT authorship contribution statement

Xiangqiang Wu: Conceptualization, Data curation, Writing – original draft, Writing – review & editing, Investigation, Validation, Methodology. **Yue Wu:** Conceptualization, Writing – review & editing, Investigation, Validation, Methodology. **Zhongting Tang:** Writing – review & editing, Supervision. **Tamas Kerekes:** Conceptualization, Writing – review & editing, Methodology, Supervision, Project administration, Software.

Declaration of competing interest

The authors declare that they have no known competing financial

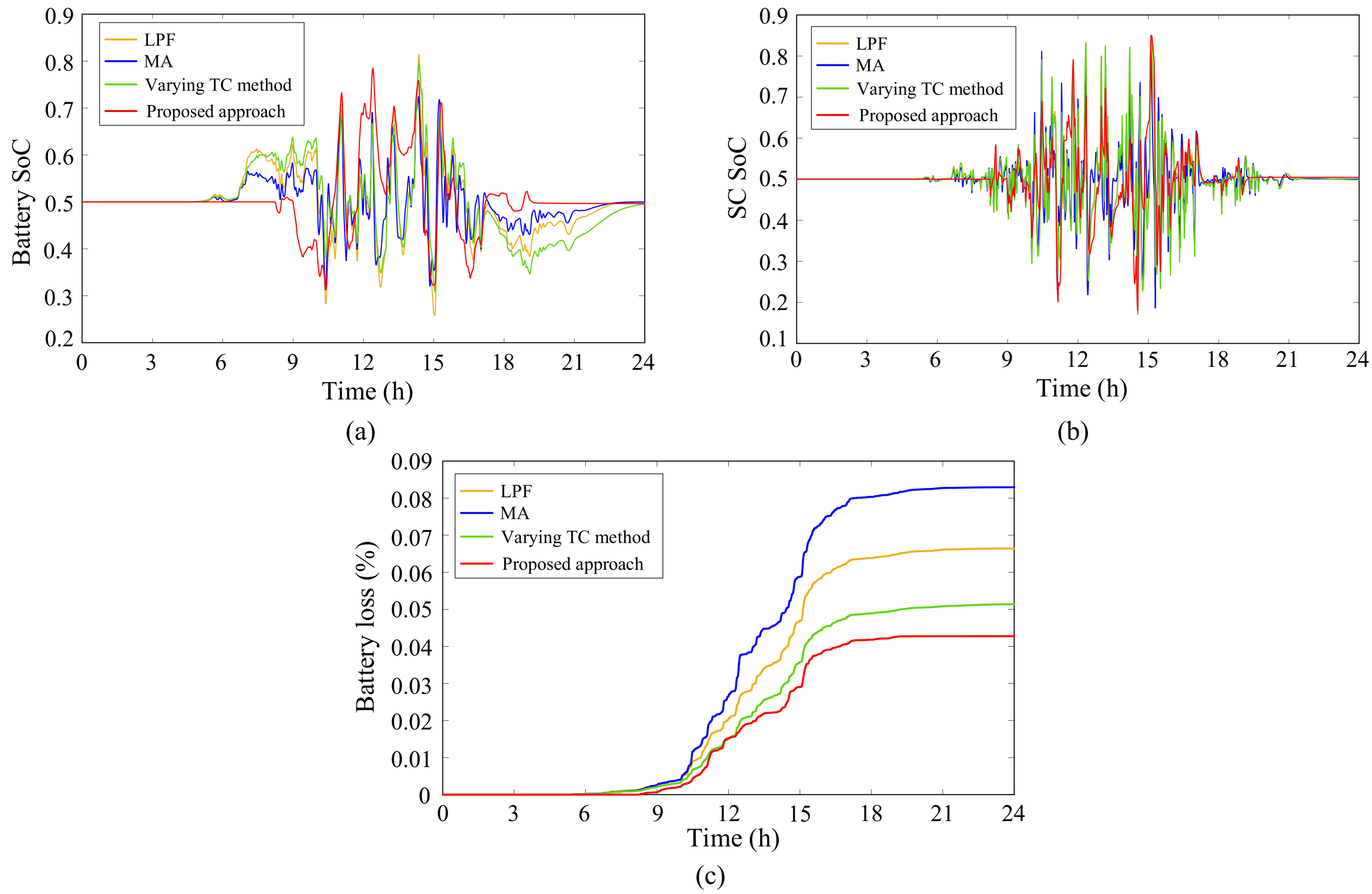

Fig. 15. Comparison of energy storage SoC and battery degradation; (a) battery SoC; (b) SC SoC; (c) battery degradation.

interests or personal relationships that could have appeared to influence the work reported in this paper.

References

[1] H. Sugihara, K. Yokoyama, O. Saeki, K. Tsuji, T. Funaki, Economic and efficient voltage management using customer-owned energy storage systems in a distribution network with high penetration of photovoltaic systems, IEEE Trans. Power Syst. 28 (1) (2012) 102–111.

[2] M. Ding, Z. Xu, W. Wang, X. Wang, Y. Song, D. Chen, A review on China′ s large-scale PV integration: Progress, challenges and recommendations, Renew. Sustain. Energy Rev. 53 (2016) 639–652.

[3] S. Sukumar, M. Marsadek, K.R. Agileswari, H. Mokhlis, Ramp-rate control smoothing methods to control output power fluctuations from solar photovoltaic (PV) sources—A review, J. Storage Mater. 20 (2018) 218–229.

[4] H.D. Tafti, G. Konstantinou, C.D. Townsend, G.G. Farivar, A. Sangwongwanich, Y. Yang, J. Pou, F. Blaabjerg, Extended functionalities of photovoltaic systems with flexible power point tracking: recent advances, IEEE Trans. Power Electron. 35 (9) (2020) 9342–9356.

[5] Bdew, Technical guideline, generating plants connected to the medium-voltage network, Germany Grid Codes (2008).

[6] The distribution code of licensed distribution network operators of Great Britain, 2018. Available from: https://www.thenbs.com/PublicationIndex/documents/details?Pub=ENA&DocID=325989.

[7] EirGrid, The grid code (version 12), 2014. Available from: chrome-extension://efaidnbmnnnibpcajpcglclefindmkaj/https://www.eirgridgroup.com/site-files/library/EirGrid/GridCode.pdf.

[8] C. Loutan, et al., Demonstration of Essential Reliability Services by a 300-MW Solar Photovoltaic Power Plant, Available from: National Renewable Energy Laboratory (NREL) (2017) https://www.nrel.gov/docs/fy17osti/67799.pdf.

[9] EgyptEra. Solar energy plants grid connection code—In addition to the Egyptian transmission grid code and the Egyptian distribution network, 2017. Available from: http://www.egyptera.org.

[10] DNV. Grid code compliance, 2016. Available from: https://www.dnv.com/services/grid-code-compliance-14319.

[11] Grid connection code for renewable power plants (RPPs). In: Connected to the Electricity Transmission System (TS) or the Distribution System (DS) in South Africa, Version 2.6. South Africa: National Energy Regulator of South Africa, NERSA; 2012. pp. 1-61.

[12] S. Shivashankar, S. Mekhilef, H. Mokhlis, M. Karimi, Mitigating methods of power fluctuation of photovoltaic (PV) sources–A review, Renew. Sustain. Energy Rev. 59 (2016) 1170–1184.

[13] H. Wen, Y. Du, X. Chen, E. Lim, H. Wen, L. Jiang, W. Xiang, Deep learning based multistep solar forecasting for PV ramp-rate control using sky images, IEEE Trans. Ind. Inf. 17 (2) (2020) 1397–1406.

[14] X. Chen, X. Xu, J. Wang, L. Fang, Y. Du, E. Lim, J. Ma, Robust proactive power smoothing control of PV systems based on deep reinforcement learning, IEEE Trans. Sustainable Energy 14 (3) (2023) 1585–1598.

[15] M.E. Şahin, F. Blaabjerg, A hybrid PV-battery/supercapacitor system and a basic active power control proposal in MATLAB/simulink, Electronics 9 (1) (2020) 129.

[16] K. Koiwa, K. Liu, J. Tamura, Analysis and design of filters for the energy storage system: Optimal tradeoff between frequency guarantee and energy capacity/power rating, IEEE Trans. Ind. Electron. 65 (8) (2017) 6560–6570.

[17] K.M. Verij, S.J. Sadati, S.A. Gholamian, Adaptive frequency control support of a DFIG based on second-order derivative controller using data-driven method, Int. Trans. Electrical Energy Sys. 30 (7) (2020) e12424.

[18] M.A. Syed, A.A. Abdalla, A. Al-Hamdi, M. Khalid, Double moving average methodology for smoothing of solar power fluctuations with battery energy storage, Int. Conf. Smart Grids Energy Sys. (SGES) 2020 (2020) 291–296.

[19] R. Kini, D. Raker, T. Stuart, R. Ellingson, M. Heben, R. Khanna, Mitigation of PV variability using adaptive moving average control, IEEE Trans. Sustainable Energy 11 (4) (2019) 2252–2262.

[20] Y. Jiao, D. Månsson, Power distribution strategy based on low-pass filter controller with a variable time constant in hybrid energy storage systems, IEEE PES Innovative Smart Grid Technol. Eur. (ISGT Europe) 2021 (2021) 1–5.

[21] A.A. Abdalla, M.S. El Moursi, T.H. El-Fouly, K.H. Al Hosani, A novel adaptive power smoothing approach for PV power plant with hybrid energy storage system, IEEE Trans. Sustainable Energy 14 (2023) 1457–1473.

[22] T. Wu, W. Yu, L. Guo, A study on use of hybrid energy storage system along with variable filter time constant to smooth DC power fluctuation in microgrid, IEEE Access 7 (2019) 175377–175385.

[23] J. Shi, L. Wang, W.J. Lee, X. Cheng, X. Zong, Hybrid energy storage system (HESS) optimization enabling very short-term wind power generation scheduling based on output feature extraction, Appl. Energy 256 (2019) 113915.

[24] X. Gao, L. Wang, T. Jin, J. Liu, Q. Liu, Research on hybrid energy storage power distribution strategy based on parameter optimization variational mode decomposition, Energy Storage Sci. Technol. 11 (1) (2022) 147.

[25] G. Xiao, F. Xu, L. Tong, H. Xu, P. Zhu, A hybrid energy storage system based on self-adaptive variational mode decomposition to smooth photovoltaic power fluctuation, J. Storage Mater. 55 (2022) 105509.
[26] T. Guo, Y. Liu, J. Zhao, Y. Zhu, J. Liu, A dynamic wavelet-based robust wind power smoothing approach using hybrid energy storage system, Int. J. Electr. Power Energy Syst. 116 (2020) 105579.
[27] W. Ma, W. Wang, X. Wu, R. Hu, F. Tang, W. Zhang, X. Han, L. Ding, Optimal allocation of hybrid energy storage systems for smoothing photovoltaic power fluctuations considering the active power curtailment of photovoltaic, IEEE Access 7 (2019) 74787–74799.
[28] S. Li, J. Zhu, H. Dong, H. Zhu, J. Fan, A novel rolling optimization strategy considering grid-connected power fluctuations smoothing for renewable energy microgrids, Appl. Energy 309 (2022) 118441.
[29] S. Hajiaghasi, A. Salemnia, M. Hamzeh, Hybrid energy storage system for microgrids applications: A review, J. Storage Mater. 21 (2019) 543–570.
[30] D. Alvaro, R. Arranz, J.A. Aguado, Sizing and operation of hybrid energy storage systems to perform ramp-rate control in PV power plants, Int. J. Electr. Power Energy Syst. 107 (2019) 589–596.
[31] Nichinte A., Vyawahare V., Magare D., Estimation and comparison of module temperature model coefficient for different PV technology module, 2020 3rd International Conference on Communication System, Computing and IT Applications (CSCITA), 2020: 13-17.
[32] J. Wang, P. Liu, J. Hicks-Garner, E. Sherman, S. Soukiazian, M. Verbrugge, H. Tataria, J. Musser, P. Finamore, Cycle-life model for graphite-LiFePO4 cells, J. Power Sources 196 (8) (2011) 3942–3948.
[33] Z. Song, H. Hofmann, J. Li, J. Hou, X. Zhang, M. Ouyang, The optimization of a hybrid energy storage system at subzero temperatures: Energy management strategy design and battery heating requirement analysis, Appl. Energy 159 (2015) 576–588.
[34] J. Sun, G. Liu, G. Tian, J. Zhang, Smart obstacle avoidance using a danger index for a dynamic environment, Appl. Sci. 9 (8) (2019) 1589.
[35] Q. Yao, Z. Zheng, L. Qi, H. Yuan, X. Guo, M. Zhao, Z. Liu, T. Yang, Path planning method with improved artificial potential field—a reinforcement learning perspective, IEEE Access 8 (2020) 135513–135523.
[36] Y. Wu, Z. Huang, H. Liao, B. Chen, X. Zhang, Y. Zhou, Y. Liu, H. Li, J. Peng, Adaptive power allocation using artificial potential field with compensator for hybrid energy storage systems in electric vehicles, Appl. Energy 257 (2020) 113983.
[37] Q. Xun, V. Roda, Y. Liu, X. Huang, R. Costa-Castello, An adaptive power split strategy with a load disturbance compensator for fuel cell/supercapacitor powertrains, J. Storage Mater. 44 (2021) 103341.
[38] J. Marcos, L. Marroyo, E. Lorenzo, D. Alvira, E. Izco, Power output fluctuations in large scale PV plants: one year observations with one second resolution and a derived analytic model, Prog. Photovolt. Res. Appl. 19 (2) (2011) 218–227.
[39] A. Maafi, S. Harrouni, Preliminary results of the fractal classification of daily solar irradiances, Sol. Energy 75 (1) (2003) 53–61.